REYNOLDS STRESS TRANSPORT MODELING FOR STEADY AND UNSTEADY CHANNEL FLOWS WITH WALL INJECTION

Bruno Chaouat
Department of Computational Fluid Dynamics and Aeroacoustics, ONERA
BP 72 - 92322 Châtillon cedex, France
Bruno.Chaouat@onera.fr

Roland Schiestel
Laboratoire IRPHE CNRS/Universités d'Aix-Marseille I & II
Château-Gombert, BP 146 - 13384 Marseille cedex 13, France
Roland.Schiestel@irphe.univ-mrs.fr

ABSTRACT

Predictions of steady and unsteady injection driven flows in a plane channel are performed by solving the averaged Navier-Stokes equations using a compressible Reynolds stress model. The boundary condition for the fluid injection through the porous wall has been formulated by taking into account experimental investigations. For the steady flow, laminar to turbulent regimes are reproduced in good agreement with the experimental data. For the unsteady flow, the resonant frequency as well as the coherent flow structures are fairly well predicted with the experiment.

INTRODUCTION

Turbulence plays a significant role in the flow in solid propellant rocket motors through its influence on the momentum and energy transfers in the motor chamber. For fluid dynamics investigations, the flow in a solid rocket motor can be produced by a duct flow with fluid injection from a porous wall. Different flow regimes occur in the duct, depending on the injection Reynolds number $R_s = u_s\delta/\nu$ where u_s, δ and ν represent the injection velocity at the permeable surface, the diameter and the kinematic viscosity (Casalis et al., 1998). The flow can evolve spatially from a laminar to a steady turbulent regime, with a transition process (Dunlap et al., 1990). It can also be oscillating due to the coupling between vortices generated by the hydrodynamic instability mechanism and the chamber acoustic modes (Flandro, 1986 and Doston, 1997). In the case where the vortices are emitted at a frequency close to the one of a longitudinal acoustic mode, the flow can be characterized by an acoustic resonant regime. For instance, large solid propellant boosters for space launchers may exhibit low pressure and thrust oscillations. These different flow regimes affect the ballistics prediction. Because of the large size of the chamber, direct numerical simulation of the whole flow domain can not be performed. Only a flow domain of the chamber has been simulated recently (Venugopal et al., 2000). Large Eddy Simulation is a promising route for studying motor internal flows that allows a good description of the turbulence interaction mechanisms (Apte and Yang, 2000). But the required computational time still remains very large. Numerical flow predictions have been made by several authors using first order turbulence models such as $k-\epsilon$ or $k-\omega$. But these models cannot give satisfactory prediction of the transition process and the turbulence levels in the post transition zone (Sviridenkov, 1976; Sabnis et al., 1989; Chaouat, 1997). Contrary to first order turbulence models, a Reynolds Stress Model provides a better description of this type of flow (Beddini, 1986). This is mainly due to the pressure-strain correlation term which has a pivotal role in redistributing turbulent energy among the Reynolds stress components. The present study is concerned with second order turbulence transport modeling of steady and unsteady flows with natural instabilities. We show that this level of closure is able to reproduce both steady and unsteady flows with a good description of the acting mechanisms.

EXPERIMENTAL SETUP

In order to analyse injection induced flows, ONERA has developed the experimental setup VECLA (Avalon, 1998). It is a plane channel bounded on one side by a porous plate made of sintered bronze and on the other side by an impermeable wall as indicated in figure (1). The size of the porosity of the porous material is 8 μm. Cold air at 303 K is injected with a uniform mass flow rate m. The length of the channel is 581 mm. By adjusting the height of the channel δ and the injection velocity u_s, different flow regimes can be realized. In particular, for $\delta = 10$ mm, $m = 2.619$ kg/m^2s, $u_s \approx 1.36$ m/s, $R_s \approx 1600$, the flow undergoes a transition process from the laminar to turbulent regime. For $\delta = 20$ mm, $m = 2.04$ kg/$m^2 s$, $u_s \approx 1.70$ m/s, $R_s \approx 2200$, the flow presents an acoustic resonant regime. It is of interest to note that linear stability theory shows that the axial-flow Reynolds number at neutral stability increases linearly for large values of the injection Reynolds number (Casalis et al., 1998). Velocity measurement have been performed with a hot wire probe located at different cross sections of the channel.

GOVERNING EQUATIONS

Turbulent flow of a viscous fluid is considered. As in the usual treatment of turbulence, the flow variable ξ is decomposed into ensemble Reynolds average and fluctuating parts as $\xi = \overline{\xi} + \xi'$. In the present case, the Favre average is used for compressible fluid so that the variable ξ can be written as $\xi = \tilde{\xi} + \xi''$ with the particular properties $\tilde{\xi''} = 0$ and $\overline{\rho\xi''} = 0$, where ρ is the mass density. These relations imply that $\tilde{\xi} = \overline{\rho\xi}/\bar{\rho}$. The Reynolds average of the Navier-Stokes equations produces in Favre variables the following forms of the mass, momentum and energy equations:

$$\frac{\partial \bar{\rho}}{\partial t} + \frac{\partial}{\partial x_j}(\bar{\rho}\tilde{u}_j) = 0 \tag{1}$$

$$\frac{\partial}{\partial t}(\bar{\rho}\,\tilde{u}_i) + \frac{\partial}{\partial x_j}(\bar{\rho}\,\tilde{u}_i\,\tilde{u}_j) = \frac{\partial \bar{\Sigma}_{ij}}{\partial x_j} \tag{2}$$

$$\frac{\partial}{\partial t}(\bar{\rho}\,\tilde{E}) + \frac{\partial}{\partial x_j}(\bar{\rho}\,\tilde{E}\,\tilde{u}_j) = \frac{\partial}{\partial x_j}\left(\bar{\Sigma}_{ij}\tilde{u}_i\right) + \frac{\partial}{\partial x_j}\left(\overline{\sigma_{ij}u_i''} - \tfrac{1}{2}\bar{\rho}\,\widetilde{u_k''u_k''u_j''}\right) - \frac{\partial \bar{q}_j}{\partial x_j} \tag{3}$$

where u_i, E, Σ_{ij}, σ_{ij}, q_i are the velocity vector, the total energy, the total stress tensor, the viscous stress tensor and the total heat flux vector, respectively. The mean stress tensor $\bar{\Sigma}_{ij}$ is composed of the mean pressure $\bar{p}$, the mean viscous stress $\bar{\sigma}_{ij}$ and the turbulent stress $\bar{\rho}\,\tau_{ij}$ as follows:

$$\bar{\Sigma}_{ij} = -\bar{p}\delta_{ij} + \bar{\sigma}_{ij} - \bar{\rho}\tau_{ij} \tag{4}$$

In this expression, the mean thermodynamic pressure is computed as:

$$\bar{p} = (\gamma - 1)\bar{\rho}\left(\tilde{E} - \tfrac{1}{2}\tilde{u}_i\tilde{u}_i - \tfrac{1}{2}\widetilde{u_i''u_i''}\right) \tag{5}$$

where γ is the ratio of specific heats c_p/c_v. The tensor $\bar{\sigma}_{ij}$ takes the usual form:

$$\bar{\sigma}_{ij} = \bar{\mu}\left(\frac{\partial \tilde{u}_i}{\partial x_j} + \frac{\partial \tilde{u}_j}{\partial x_i}\right) - \frac{2}{3}\bar{\mu}\frac{\partial \tilde{u}_k}{\partial x_k}\delta_{ij} \tag{6}$$

where the Favre-averaged Reynolds stress tensor is $\tau_{ij} = \widetilde{u_i''u_j''}$ and μ is the molecular viscosity. The mean heat flux $\bar{q}_i$ is composed of the laminar and turbulent flux contributions:

$$\bar{q}_i = -\bar{\kappa}\frac{\partial \tilde{T}}{\partial x_i} + \bar{\rho}\,\widetilde{h''u_i''} \tag{7}$$

where T, h and κ are, respectively, the temperature, the specific enthalpy and the thermal conductivity. Closure of the mean flow equations is necessary for the turbulent stress $\bar{\rho}\,\widetilde{u_i''u_j''}$, the turbulent transport of the turbulent kinetic energy $\bar{\rho}\,\widetilde{u_k''u_k''u_j''}$, and the turbulent heat flux $\bar{\rho}\,\widetilde{h''u_i''}$. The Favre-averaged correlation tensor $\tau_{ij} = \widetilde{u_i''u_j''}$ is computed by the Reynolds stress model of Launder and Shima (1989) which has been extended for compressible flows and modified for predicting flows with fluid injection through a porous wall (Chaouat, 2000). This model is selected because its formulation is simpler and requires less empirical adjustment than most other models. So it is a good canditate to handle a large variety of flows. It has predicted rotating channel flows fairly well (Chaouat, 2001). The transport equation of the Reynolds stress tensor is:

$$\frac{\partial}{\partial t}(\bar{\rho}\,\tau_{ij}) + \frac{\partial}{\partial x_k}(\bar{\rho}\,\tau_{ij}\tilde{u}_k) = J_{ij} + P_{ij} - \frac{2}{3}\bar{\rho}\epsilon\delta_{ij} - c_1\bar{\rho}\epsilon a_{ij} + \Phi_{ij}^2 + \Phi_{ij}^w \tag{8}$$

where :

$$J_{ij} = \frac{\partial}{\partial x_k}\left(\bar{\mu}\frac{\partial \tau_{ij}}{\partial x_k} + c_s\bar{\rho}\frac{k}{\epsilon}\tau_{kl}\frac{\partial \tau_{ij}}{\partial x_l}\right) \tag{9}$$

$$P_{ij} = -\bar{\rho}\tau_{ik}\frac{\partial \tilde{u}_j}{\partial x_k} - \bar{\rho}\tau_{jk}\frac{\partial \tilde{u}_i}{\partial x_k} \tag{10}$$

$$\Phi_{ij}^2 = -c_2\left(P_{ij} - \tfrac{1}{3}P_{kk}\delta_{ij}\right) \tag{11}$$

$$\Phi_{ij}^w = c_1^w\frac{\bar{\rho}\epsilon}{k}(\tau_{kl}n_kn_l\delta_{ij} - \tfrac{3}{2}\tau_{ki}n_kn_j - \tfrac{3}{2}\tau_{kj}n_kn_i)f_w + c_2^w(\Phi_{kl}^2n_kn_l\delta_{ij} - \tfrac{3}{2}\Phi_{ik}^2n_kn_j - \tfrac{3}{2}\Phi_{jk}^2n_kn_i)f_w \tag{12}$$

The terms on the right-hand side of equation (8) are identified as diffusion, production by the mean flow, dissipation, slow redistribution, rapid redistribution and wall reflection. In these expressions, $k = \tau_{ii}/2$ is the turbulent kinetic energy, $a_{ij} = (\tau_{ij} - \frac{2}{3}k\delta_{ij})/k$ is the anisotropy tensor, c_1, c_2, c_1^w, c_2^w are functions which depend on the second and third invariants $A_2 = a_{ij}a_{ji}$, $A_3 = a_{ij}a_{jk}a_{ki}$, the flatness coefficient parameter $A = 1 - \frac{9}{8}(A_2 - A_3)$ and the turbulent Reynolds number $R_t = k^2/\nu\epsilon$. The dissipation rate ϵ in expression (8) is computed by means of the transport equation:

$$\frac{\partial}{\partial t}(\bar{\rho}\epsilon) + \frac{\partial}{\partial x_j}(\bar{\rho}\tilde{u}_j\epsilon) = J - (c_{\epsilon 1} + \psi)\bar{\rho}\frac{\epsilon}{k}\tau_{ij}\frac{\partial \tilde{u}_j}{\partial x_i} - c_{\epsilon 2}\bar{\rho}\frac{\tilde{\epsilon}\epsilon}{k} \tag{13}$$

where

$$J = \frac{\partial}{\partial x_i}\left(\bar{\mu}\frac{\partial \epsilon}{\partial x_i} + c_\epsilon\bar{\rho}\frac{k}{\epsilon}\tau_{ij}\frac{\partial \epsilon}{\partial x_j}\right) \tag{14}$$

and $\tilde{\epsilon} = \epsilon - 2\nu(\partial\sqrt{k}/\partial x_2)^2$. The diffusive terms are modeled by a gradient hypothesis:

$$\overline{\sigma_{ij}u_i''} - \frac{1}{2}\bar{\rho}\,\widetilde{u_k''u_k''u_j''} = (\bar{\mu}\delta_{jm} + c_s\bar{\rho}\frac{k}{\epsilon}\tau_{jm})\frac{\partial k}{\partial x_m} \tag{15}$$

The heat transfer of the turbulent flux is computed as:

$$\widetilde{h''u_i''} = -\frac{c_\mu k^2}{\epsilon}\frac{c_p}{P_{r_t}}\frac{\partial \tilde{T}}{\partial x_i} \tag{16}$$

where c_p and P_{r_t} are the specific heat at constant pressure and the turbulent Prandtl number, respectively. The functions used in that model are listed in table 1. Values of the constant coefficients are $c_s = 0.22$, $c_{\epsilon 1} = 1.45$, $c_{\epsilon 2} = 1.9$, $c_\epsilon = 0.18$, $c_\mu = 0.09$.

NUMERICAL METHOD

The finite volume technique is used to solve the full equations incorporating all the derivative terms.

c_1	$1+2.58AA_2^{\frac{1}{4}}(1-\exp(-(0.0067R_t)^2))$
c_2	$0.75A^{\frac{1}{2}}$
c_1^w	$-\frac{2}{3}c_1+1.67$
c_2^w	$\max(\frac{2}{3}c_2-\frac{1}{6},0)/c_2$
f_w	$0.4k^{\frac{3}{2}}/\epsilon x_2$
ψ	$-c_{\epsilon 1}/8 < 1.5A\left(\frac{P_{ii}}{2\bar{\rho}\epsilon}-1\right) < c_{\epsilon 1}/8$

Table 1: Functions used in the RSM model.

The numerical discretization scheme is second-order accurate in space and the time advancement uses a three-step Runge-Kutta method which is appropriate for simulating unsteady flows. A pressure boundary condition is applied at the exit section of the channel. Boundary conditions for impermeable walls assume zero velocity and constant temperature, zero turbulent kinetic energy and the wall dissipation rate value $\epsilon_w = 2\nu(\partial\sqrt{k}/\partial x_2)^2$. For a permeable wall, a constant mass flow rate is imposed at the same temperature as the impermeable wall. Experimental measurements in the immediate vicinity of the permeable wall show that the velocity follows a Gaussian distribution. Investigations indicate also that the amplitude of the fluctuating velocity increases with increasing injection velocity (Avalon, 1998). From a physical point of view, the fluctuating part of the velocity is due to the injected fluid passing through the porous plate made of small bronze spheres and by the acoustics of the cavity. Based on these considerations, the boundary condition has been modeled by a twofold hypothesis. The first effect is taken into account by introducing a modeled turbulence level at the wall related to the mean injected velocity as $\sigma_s = (\widetilde{u_2''u_2''}/\tilde{u}_s^2)^{1/2}$. It is assumed that the material porosity is fine grained ($8\mu m$). The second effect which is not a turbulent effect is produced by a forcing with a Gaussian velocity distribution $P(u)$ in time but constant in space. The forcing is thus applied directly to the near wall mean velocity. Another point to emphasize concerns the pressure fluctuations of the flowfield. Considering that the permeable wall does not reflect the pressure fluctuations, the term Φ_{ij}^w of equation (12) is suppressed in the direction normal to the wall.

NUMERICAL RESULTS

Steady flow regime

Numerical flow predictions are performed on a mesh requiring 100 x 100 non-uniform grid points in x_1 and x_2 directions. The objective is to reproduce the steady flow which evolves spatially from laminar to turbulent regimes. Due to the mass conservation equation, the flow Reynolds number $R_m = \rho_m u_m \delta/\mu$ based on the bulk density ρ_m and the bulk velocity u_m varies linearly with the axial distance along the channel so that it can be computed as $R_m = mx_1/\mu$. It ranges from zero to approximately 9 x 10^4. In this work, different values of the coeffcient σ_s are considered. As a result, it is found that the effect of turbulence in injected fluid is to delay or to anticipate the transition process of the flow. This is illustrated in Figure (2) which shows, for different values of the injection paramater σ_s, the evolution of the integral momentum flux coefficient defined by :

$$\beta = \frac{\rho\delta\int_0^\delta \bar{\rho}\tilde{u}_1^2 dx_2}{\left(\int_0^\delta \bar{\rho}\tilde{u}_1 dx_2\right)^2} \tag{17}$$

The rapid drop of the coefficient β corresponds to the transition location. It can be noticed that the lower turbulence level $\sigma_s = 0.1$ is too small to trigger the transition process. This Figure reveals a qualitative agreement with the experimental data. Figure (3) shows the evolution of the dimensionless mean velocity profiles in different sections of the channel for the computation using $\sigma_s = 0.2$. The profile located in the section $x_1 = 22$ cm appears to be quite laminar whereas the profiles corresponding to the sections at 45 cm and 57 cm are found to be turbulent. The general shapes of the profiles display a good agreement with experimental data. Figure (4) and Figure (5) show, respectively, the streamwise and normal turbulent velocity fluctuations normalized by the bulk velocity $(\widetilde{u_1''u_1''})^{1/2}/u_m$, $(\widetilde{u_2''u_2''})^{1/2}/u_m$ in different sections. One can observe that the RSM model predicts fairly well the turbulence intensity which evolves from zero to approximately ten percent of the bulk velocity u_m. Note that previous computations of this flow using the $k-\epsilon$ model have overpredicted the turbulence intensity by about 300 % in the post-transition zone (Chaouat, 2000).

Unsteady flow regime

Several predictions of the oscillatory flowfield with natural instabilities are performed on meshes taking into account 600 x 100 non-uniform grids. For the computation, 2 $\times 10^6$ temporal iterations which represents 0.2 s of time are made. The experimental signal pressure spectrum plotted in Figure (6) indicates that the flow presents a resonant regime at the frequency $f = 407$ Hz (Avalon et al., 1998). This is quite close to the frequency $f = 3a_o/4L = 426$ Hz which corresponds to the second longitudinal acoustic mode $3\lambda/4$. The quantity a_o denotes the sound velocity. Indeed, visualisation tests (Avalon et al., 2000) show the emission of flowfield vortices at this frequency. Therefore, the flow is characterized by an acoustic resonant regime. In general, the wave length solutions of the Helmholtz equation are $\lambda = 4L/(2n+1)$ and the frequencies are $f = (2n+1)a_0/4L$. For the values $n = 0, 1, 2$, the first frequencies are 142, 426 and 711 Hz. It can be mentionned that the dimensionless resonant frequency is $\Omega^* = 2\pi\delta f/u_s = 30$ whereas the dimensionless critical frequency obtained by the linear stability analysis is $\Omega_c^* \approx 18.5$ (Casalis et al., 1998). In the computation, the Gaussian forcing has been artificially generated through fluctuating velocities $u_1' = \alpha\bar{u_1}P_1$, $u_2' = \alpha\bar{u_2}P_2$ where P_1 and P_2 are Gaussian distributions and the quantity α is a numerical coefficient. These distributions are obtained by $P_1 = t_1\cos(2\pi t_2)$ and $P_2 = t_1\sin(2\pi t_2)$, where $t_1 = \sqrt{-2\ln t_3}$, t_2 and t_3 are uniform random numbers in the interval [0,1] (Knuth, 1998). The distribution of the probability function P_1, (similary for P_2), is represented on Figure (7) for 10^6 events. In order to

reproduce the level of the experimental noise, the coefficient α is assigned a value 0.02. As for the previous steady flow prediction, an injected turbulence intensity $\widetilde{u_2''u_2''}$ related to the porous material properties is also introduced at the wall. One result of interest is that the flow regime remains stable if no Gaussian forcing is imposed in the flowfield, regardless the intensity of the injected turbulence. Therefore, in order to trigger the instabilities, the Gaussian forcing has been applied and periodically refreshed in the immediate vicinity of the permeable wall. Lupoglazoff and Vuillot (1998), in order to simulate this flow in laminar regime, also have to trigger the instabilities by injected noise. The present computed unsteady pressure signal is plotted on Figure (8). Figure (9) shows the head-end pressure spectrum that reveals the presence of the mode $3\lambda/4$. The fluctuating pressure peaks occur at 403 Hz and 422 Hz, with a resolution frequency of 5 Hz. The following modes $\lambda/4$, $7\lambda/4$ and $9\lambda/4$ are also observed on this Figure. Although the resonance frequency is well predicted, a discrepancy in the magnitude of the pressure fluctuations is observed between the experimental and computed signals in Figures (6) and (9). This is due to the poral response or admittance which consists in adjusting the injected mass flow rate as a function of the local pressure (Lupoglazoff and Vuillot, 1998). However, in the present work, a zero poral response has been considered for the sake of simplicity which should explain the over-estimated level. Figure (10) shows the instantaneous vorticity contours in the whole flow domain in the real scale. The development of the acoustic boundary layer as well as the parietal vortex shedding which results from natural instabilities can be observed in the channel. Figure (11) shows the enlarged view of the instantaneous vorticity contours near the exit of the channel and reveals the flow structures. Figure (12) describes the instantaneous entropy contours and illustrates the coherent eddies of the flowfield. Figure (13) shows the contours of the turbulent Reynolds number and reveals that the turbulence is mostly developed near the impermeable wall. It is of interest to mention that the $k-\epsilon$ model with the same conditions at the boundaries (Chaouat and Schiestel, 2001) failed to reproduce the large scale structures of the flow because of its dissipative behavior (see Figure 14).

CONCLUSION

An advanced second-order turbulence model has been used to predict flows with complex physics, such as strong effects of the streamlines curvature due to the fluid injection, different flow regimes from laminar to turbulent and the transition, unsteady flow involving an acoustic resonance. Both steady and unsteady flows are fairly well predicted in comparison with the experiments. In particular for the unsteady flow, it has been demonstrated that the RSM turbulence model is able to reproduce the vortex shedding mechanism which results from natural instabilities and has been visually observed.

References

Apte, S. and Yang, V., 2000, "Large Eddy Simulation of Internal Flowfield in Porous Chamber with Surface Mass Injection", *38th AIAA Aerospace Sciences Meeting and Exhibit*, paper 0729.

Avalon, G., Casalis, G. and Griffond, J., 1998, "Flow Instabilities and Acoustic Resonance of Channels with Wall Injection", *34th AIAA Joint Propulsion Conference and Exhibit*, AIAA paper 3218.

Avalon, G., Ugurtas, B.,Grish, F., 2000, "Numerical Computations and Visualization Tests of the Flows Inside a Cold Gas Simulation with Characterization of a Parietal Vortex Shedding", *36th AIAA Joint Propulsion Conference and Exhibit*, paper 3387.

Beddini, R. A., 1986, "Injection-Induced Flows in Porous-Walled Ducts", *AIAA Journal*, Vol. 11, pp. 1766-1773.

Casalis, G., Avalon, G. and Pineau, J. P., 1998, "Spatial Instability of Planar Channel Flow with Fluid Injection through Porous Walls", *Physics of Fluid*, Vol. 10, pp. 2558-2568.

Chaouat, B., 1997, "Computation using $k-\epsilon$ Model with Turbulent Mass Transfer in the Wall Region", *11th Symposium on Turbulence Shear Flows*, Vol. 2, pp. 2.71-2.76.

Chaouat, B., 2000, "Numerical Simulations of Channel Flows with Fluid Injection Using a Reynolds Stress Model", *38th AIAA Aerospace Sciences Meeting and Exhibit*, paper 0992.

Chaouat, B., 2001, "Simulations of Channel Flows with Effects of Spanwise Rotation or Wall Injection Using a Reynolds Stress Model", *ASME Journal of Fluid Engineering*, Vol. 123, pp. 1-9.

Chaouat, B. and Schiestel, R., 2001, Prévision d'écoulements instationnaires de canal soumis à une injection pariétale par un modèle RSM. Technical Report 4/6174 DSNA, ONERA.

Doston, K. W., 1997, "Vortex Shedding in a large Solid Rocket Motor Without Inhibitors at the Segment Interfaces", *Journal of Propulsion and Power*, Vol. 13, pp. 197-206.

Dunlap, R., Blackner, A. M, Waugh, R. C., Brown, R. S. and Willoughby, P. G, 1990, "Internal Flow Field Studies in a Simulated Cylindrical Port Rocket Chamber", *Journal of Propulsion and Power*, Vol. 6, pp. 690-704.

Flandro, G. A., 1986, "Vortex Driving Mechanism in Oscillatory Rocket Flows", *Journal of Propulsion and Power*, Vol. 2, pp. 206-214.

Knuth, D. E., 1998, "The Art of Computer Programming", *Addison-Wesley Publishing Company.*

Lupoglazoff, N. and Vuillot, F, 1998, "Numerical Simulations of Parietal Vortex shedding Phenomenon in a Cold Flow Set-up", *34th AIAA Joint Propulsion Conference and Exhibit*, paper 3220.

Sabnis J. S., Madabhushi, R. K and McDonald, H., 1989, "Navier-Stokes Analysis of Solid Propellant Rocket Motor Internal Flows", *AIAA Journal*, Vol. 5, pp. 657-664.

Sviridenkov, A. A. and Yagodkin, V. I, 1976, "Flows in the Initial Sections of Channels with Permeable Walls", *Fluid Dynamics*, Vol. 11, pp. 43-48.

Venugopal, P., Najjar F. M. and Moser, R. D., 2000, "DNS and LES Computations of Model Solid Rocket Motors", *36th AIAA Joint Propulsion Conference and Exhibit*, paper 3511.

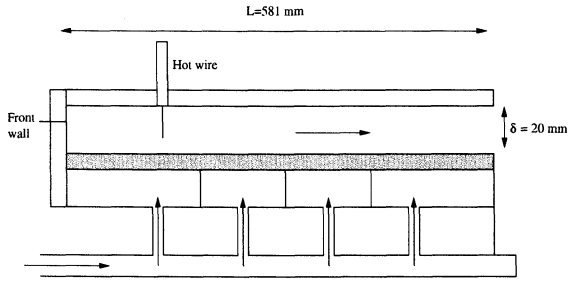

Figure 1: Sketch of VECLA facility

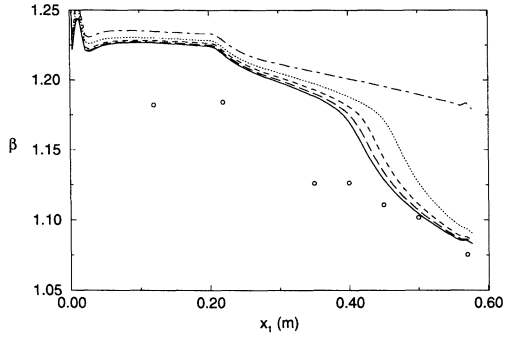

Figure 2: Axial variations of the coefficient β. $\circ$: experimental data. dot-dashed-line: $\sigma_s = 0.1$, dotted-line: $\sigma_s = 0.2$, dashed-line: $\sigma_s = 0.3$, long-dashed-line: $\sigma_s = 0.4$, solid-line: $\sigma_s = 0.5$

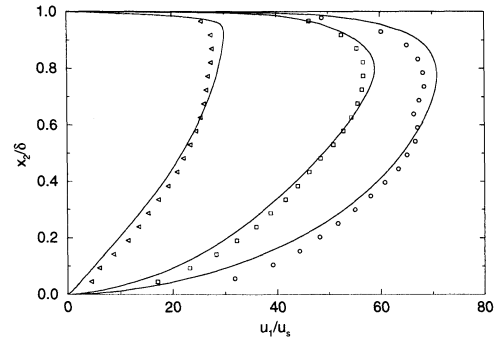

Figure 3: Mean dimensionless velocity profiles in different sections. $\sigma_s = 0.2$; Symbols: experimental data; solid line: RSM. 22 cm: $\triangleleft$; 45 cm: $\square$; 57 cm: $\circ$.

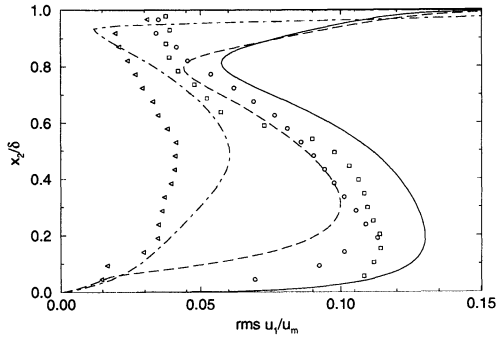

Figure 4: Turbulent velocity fluctuations normalized by the bulk velocity in different sections; $(\widetilde{u_1'' u_1''})^{1/2}/u_m$. $\sigma_s = 0.2$. $x_1 = 22$ cm: $\triangleleft$, dot-dashed line; 45 cm: $\square$, dashed line; 57 cm: $\circ$, solid line.

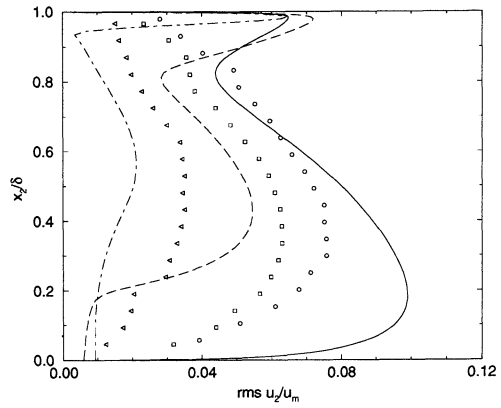

Figure 5: Turbulent velocity fluctuations normalized by the bulk velocity in different sections; $(\widetilde{u_2'' u_2''})^{1/2}/u_m$. $\sigma_s = 0.2$. $x_1 = 22$ cm: $\triangleleft$, dot-dashed line; 45 cm: $\square$, dashed line; 57 cm: $\circ$, solid line.

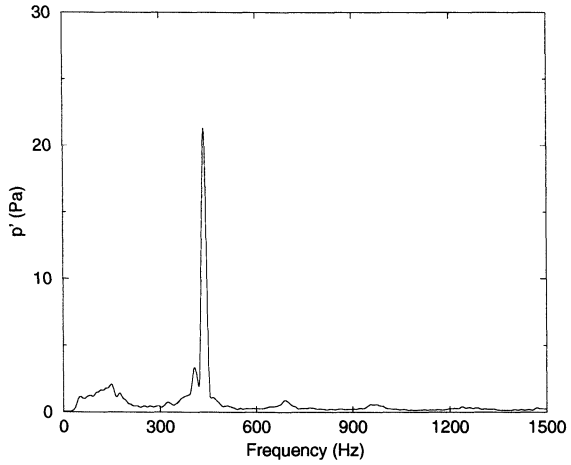

Figure 6: Experimental head end presssure spectrum

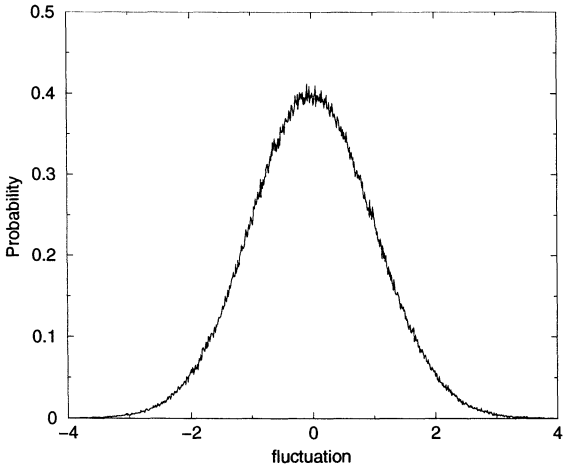

Figure 7: Gaussian probability for the fluctuating velocity.

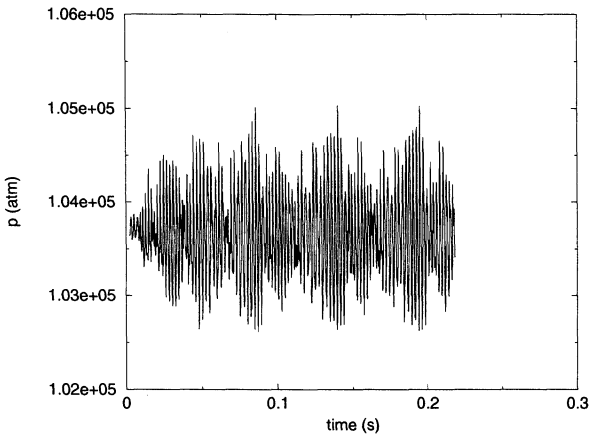

Figure 8: Head end pressure evolution versus time.

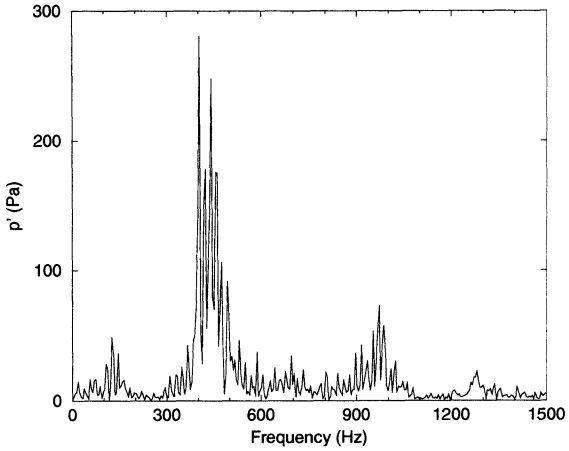

Figure 9: Head end pressure spectrum.

Figure 10: View of the instantaneous vorticity contours in real aspect ratio.

Figure 11: Enlarged view of the instantaneous vorticity contours.

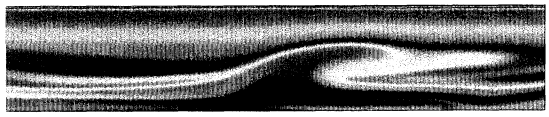

Figure 12: Enlarged view of the instantaneous entropy contours.

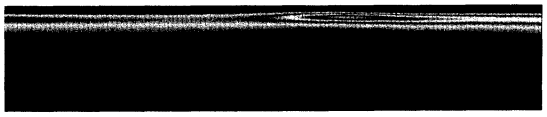

Figure 13: Enlarged view of the turbulent Reynolds number contours $R_t = k^2/\nu\epsilon$. $0 < R_t < 1620$.

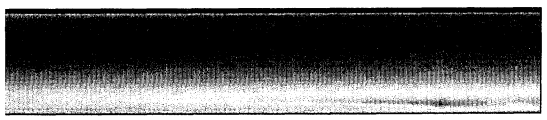

Figure 14: Enlarged view of the instantaneous vorticity contours for the $k - \epsilon$ model.